

Photo-electrochemical reduction of CO₂ to Methanol on Quaternary chalcogenide loaded Graphene-TiO₂ ternary nanocomposite fabricated via Pechini method

Zambaga Otgonbayar

Won-Chun Oh (✉ wc_oh@hanseo.ac.kr)

<https://orcid.org/0000-0002-0154-7388>

Research Article

Keywords: Quaternary semiconductor, graphene, ternary nanocomposite, photocatalytic, electrochemical, Faraday efficiency

Posted Date: February 9th, 2022

DOI: <https://doi.org/10.21203/rs.3.rs-1328721/v1>

License:  This work is licensed under a Creative Commons Attribution 4.0 International License.

[Read Full License](#)

Version of Record: A version of this preprint was published at Journal of Inorganic and Organometallic Polymers and Materials on April 8th, 2022. See the published version at <https://doi.org/10.1007/s10904-022-02319-8>.

Abstract

Nano-sized catalysts have been widely studied for CO₂ reduction to hydrocarbon fuels. Herein, we study the new-modeled ternary nanocomposite that can use in photocatalytic and electrochemical CO₂ reduction. In order to adjust the energy of the catalyst band and the characteristics of the effective charge carrier, we firstly synthesized the AgFeNi₂S₄ quaternary nanocomposite and then used it to model the ternary nanocomposites, and all the nanocomposites were synthesized using the Pechini method. The activity of the nanocomposites is directly related to the output of methanol productions. In a photocatalytic CO₂ reduction experiment, the methanol yield under UV radiation was 8.679, 6.349, 4.136%, and under Vis-light it was 6.291, 4.738, and 2.339%, respectively. The stability and reusability of the catalysts are the main factors that can define the sturdiness of a photocatalyst in practical applications. The sturdiness of the catalyst has been tested four times by recycling tests, and as a result, the yield of the final product (methanol) has not decreased, confirming the stability of the catalyst. In electrochemical CO₂ reduction, the Faraday efficiency is the main parameter that defines the performance of the working electrode and the evolution of methanol. The Faraday efficiency of the AFNSGT ternary nanocomposite was 44.25%; this is an increase in the value of the Faraday efficiency, which proves that the design of the new nanocomposite successfully increases the activity of the working electrode and has a positive effect on the electrochemical reduction of CO₂. The photocatalytic and electrochemical CO₂ reduction data show that the preparation method, morphological state, and charge carrier properties of the photocatalyst are important for the catalytic activity and efficiency of the methanol evolution pathway.

1. Introduction

Industrial development is increasing both the use of fossil fuels and the amount of carbon dioxide and air pollution [1–5]. The simplest and most commonly used solution to these problems is a photocatalyst-based process. Crystal structure, nanoparticle size, band structure, and charge transfer are the main parameters that determine the catalytic activity of a photocatalyst, and these values vary depending on the synthetic method [6–8]. Many different methods are used to synthesize photocatalysts, such as the sol-gel, hydrothermal, combustion and ultrasonic-assisted methods [9–15]. Among them, the Pechini method, which is a type of modified sol-gel method, allows control of the particle size and stoichiometry. The basic process is chelation based on alpha-hydroxide carboxylic acid and organic solvents to form a metal chain by creating chemical interactions between metals and organic molecules [16].

The transition metal chalcogenide is mainly used in the practical application field because it has unique properties. Lately, some chalcogenide nanomaterial like WS₂, CoS, MoS₂, CuS and NiS₂ have materialize as a co-catalyst material. Among them, nickel sulfide serves as a high stabilized co-catalyst, as it has low Fermi-level energy with kinetic enhancement that related to the protract the life-time of electrons and push the reduction reaction on the catalyst [17–20]. Lately, the quaternary-structured nanoparticles are attracting attention because it offers to lead the adjustments of bandgap energy levels. Based on this

phenomenon, NiS₂ was uniformly combined with Ag and Cu-transition metals by a Pechini method to form the quaternary nanocomposites, and moreover, this quaternary nanocomposite was used for the synthesis of binary and ternary nanocomposites. The two transition metals have strong candidate, such as, Ag metal can apply as an electron-capture and that can enhance the light-absorption feature and partial current density with significant effect on Faradaic efficiency [21]. The copper has high conductivity and it is competent to produce the hydrocarbons, such as CO [22], CH₄ [23] and alcohol [24] that mainly depend on the potential. In addition, 2D graphene and titanium oxide (TiO₂) photocatalysts are widely studied in CO₂ reduction due to their physical and chemical properties. Compared with 0D and 1D nanomaterials, 2D-structured graphene has better catalyst activity and it has high surface area and charge transfer capacity to support the potential of the nanocomposites [25–27]. Meanwhile, the TiO₂ offers a strong oxidizing ability and good physical stability, but this semiconductor material is only activated in the UV region (< 387 nm) and is subject to the rapid convergence of electrons and holes due to its band gap energy (3.20 eV) [28]. Previous studies have shown that the graphene-TiO₂ binary photocatalyst material showed high conversion efficiency for CO₂ under light irradiation. Graphene can strengthen the physical and chemical stability of the metal-junctioned binary material and able to be a bridge between semiconductors to enhance the degree of photogenerated charge transfer [29]. Due to the strong light absorption rate and charge carrier, the ternary nanocomposites have better advantages over binary nanocomposites. Because the combinations of two or more semiconductors offer to adjust the band structure, efficient charge transport, and activity; these properties have allowed nanomaterials to find a range of new applications [30, 31]. Based on this uniqueness, our research study proposes a new modeled ternary nanocomposite that included the 2D-graphene, TiO₂, and AgFeNi₂S₄. The catalytic activity of the ternary nanocomposite was evaluated based on the conversion of CO₂ to hydrocarbon fuels.

In our previous study, we reported the solvothermal method on AgFeNi₂S₄-Graphene-TiO₂ ternary nanocomposite and used for the photocatalytic CO₂ reduction to methanol. Due to the morphology state and synthesis method, the ternary nanocomposite exhibited the high methanol production rates (8.62% AND 7.23%) under the UV-light irradiations. In this study, the AgFeNi₂S₄-Graphene-TiO₂ ternary nanocomposite was prepared by the Pechini method, which has the advantage of allowing to control of stoichiometry and particle size in the form of a chemical chain between metal and organic molecules. The prepared nanocomposite used for the CO₂ reduction, such as photocatalytic and electrochemical. This two methods have been shown to be effective due to its simplicity and ability to operate under ambient circumstances [32]. Typically, the catalyst and stable electrode are indispensable for the electrochemical CO₂ reduction, and about the process, the catalyst promotes the electron transfer from the working electrode to reductant gas (CO₂) and diminished the overpotentials. Photocatalytic CO₂ reduction processes require catalysts, sacrificial electron donors, and light sources. In the main process, the catalyst was activated by photon energy, during which the reductant gas is absorbed by the catalyst, and the excited electrons are used to reduce the CO₂ as a hydrocarbon fuel. The electron-donor scavenger allows combining the CO₂ with water and can provide sufficient cyclic electrons to the CO₂ conversion

process [33], thus supporting the production yields of methanol. Over and above that, the carbon dioxide conversion rate depends on several fundamental factors, such as the surface and morphology of the nanocomposite, composition and experimental conditions. A 0.04M NaHCO₃ solution was used in the CO₂ reduction test and used as an electrolyte for electrochemical tests to enhance the catalytic current and lessen the overpotential and as a hydrogen generator for photocatalytic tests.

Herein, the ternary nanocomposite exhibited the higher methanol production yield under UV-light and had sturdiness during the long time recycling test. Moreover, AFNSGT NCs showed that it is suitable for the methanol production from electrochemical CO₂ reduction at low potential rate with high current density value (mA/cm²).

2. Experimental

2.1. Materials

AgNO₃ (≥ 98%), Fe(NO₃)₃·9H₂O (99.9%), Ni(NO₃)₂·6H₂O (≥ 99%), Na₂S₂O₃ (≥ 99%), and C₆H₈O₇ (≥ 99.5%) were procured from Duksan Pure Chemical Co. Ltd (Korea). HCl (36 wt%), H₂SO₄ (≥ 97%), Zn(NO₃)₂·6H₂O (≥ 99.5%), and Na₂SO₃ (97%) were procured from Samchun Pure Chemical Co. LTD (Korea). Natural graphite powder is a precursor of graphene. All chemical reagents were of analytical grade and organic solvents were used with deionized water.

2.2. Synthesis

2.2.1. Preparation of AgFeNi₂S₄ quaternary nanoparticles (AFNS NPs)

The quaternary nanoparticles were synthesized by the Pechini method. The precursor solution was prepared using a 3:2 ratio of ethylene glycol (C₂H₆O₂) and chelate-cationic citric acid (C₆H₈O₇). The precursor agents of the Ag, Fe, Ni and S, in a mmol ratio of 0.02:0.03:0.04:0.08, were dispersed into the citric acid solvent and stirred at 60°C for 6 h until it became viscous. The process of preparing the mortar is called chelating, and its main function is to establish a chemical bond between the transition metal and the organic molecules in order to adjust the metal chain. The mixture was transferred into 100 ml Teflon-linedclave and heated at 150°C for 15 h, then allowed to cool to room temperature (25°C). The final product was washed with DI water and dried at 100°C, then the powder was calcined at 700°C for 2 h. The final nanoparticles were denoted as AFNS NPs. Under the same experiment conditions, Ag₂NiS₂ and FeNiS₂ were also obtained for comparison without adding the Ag or Fe, and labeled as ANS and FNS, respectively.

2.2.2. Preparation of binary and ternary nanocomposite

The binary and ternary composites were prepared by the Pechini method. The graphene was prepared by Hummer and Offerman's method [34], the details of which were described previously [35]. First, the organic solvent was prepared using absolute ethanol and DI water (volume ratio = 5:4) with continuous stirring at room temperature. Then, 0.7 g of AFNS was added to the solvent and stirred for 1 h. Graphene (0.7 g) was added to the mixture, which was stirred at 120°C for 6 h, then transferred to a 100 ml Teflon-lined stainless-steel autoclave and heat-treated at 150°C for 15 h before being cooled to 25°C. The final product was rinsed with DI water, dried completely at 90°C, and then calcined at 700°C for 2 h. The prepared sample was denoted AFNSG NCs. In the next step, TiO₂ was combined with AFNSG. The reactants were combined in a molar ratio of ethanol to H₂O to TNB of 30 : 15 : 4 and stirred continuously for 1 h. One-half gram of AFNSG nanocomposite was added to the prepared solution, which was stirred at room temperature for 6 h, then transferred to an autoclave and kept in an electric oven at 150°C for 15 h. The obtained product was rinsed with DI water and dried until it became a powder and calcined under the same conditions. The final sample was renamed as AFNSGT NCs. The morphology state and electrochemical analysis method was detail explained in the supplementary material.

2.3. Reduction process

2.3.1. Photocatalytic CO₂ reduction

The photoreduction of CO₂ was conducted in a three-part closed reactor under light irradiation (Scheme S1). The electron-donor scavenger was used in this experiment, which provided a supply of cyclic electrons to increase the catalytic activity of the photocatalyst. First, a 0.04 M NaHCO₃ solution was prepared. Then, 0.1 g of photocatalyst and scavenger were dispersed in solvent and stirred for 1 h. A highly pure input gas (CO₂, 99.99%) was purged into the mixture to obtain a gas/solvent mixture; the gas was controlled by the mass flow controller and the total purging time was 30 min. Next, pure nitrogen was purged into the mixture to remove the gas from the glass reactor. The lamp was then switched on and the light source (500 W halide lamp) was placed at the top of the reactor at a distance of about 10 cm. In detail, 100 mg of photocatalyst and 0.3 g scavenger were dispersed in 0.04 M NaHCO₃ containing 50 ml solvent and stirred for 1 h. The pure input gas was controlled by the mass flow controller and the total gas-purging time was 30 min. The total reaction time was 48 hours; every 12 hours, a certain volume of solution was withdrawn from the reactor using a syringe, and the solution was filtered through a membrane filter with a pore size of 0.45 μm and a diameter of 47 mm. The amount of alcohol in the solution was analyzed using a "Quantitative analysis of alcohol" method. In this method, 10 ml of 0.1 M CrO₃ was added to a 1 ml sample and agitated for 15 min, then the suspension was centrifuged (10000 ppm/15 min). The concentration of the acquired solution was examined by a UV spectrophotometer (Optizen POP, Korea) using a quartz cell (1 × 4.5 cm). The functional group of the final methanol was analyzed by a FTIR spectrometer (FTIR iS5, Thermoscience).

2.3.2. Electrochemical CO₂ reduction

The electrochemical CO₂ reduction process was conducted on a PGP201 Potentiostat (A41A009) using a three-electrode system. Ag/AgCl and platinum were used as the reference and counter electrode, respectively. The as-prepared binary and ternary nanocomposites were used for the working electrode (WE) preparation. The WE were prepared by following the “Doctor blade” method [36]. Ethyl cellulose was used as a binding material and mixed with the as-prepared nanocomposite in a 1:3 ratio. Then, a few drops of pure ethanol were added, and the resulting mixture was ground and used to veneer the top of the Ni foil. The electrode preparation process is presented in Scheme S2. The current density determines the amount of electric current per unit cross-section of the material. The input CO₂ gas-purging speed and the amount of gas were controlled by the mass-flow controller and 50 ml of 0.04 M NaHCO₃ solvent was used as the electrolyte solution. The cyclic voltammetry (CV) measurement was conducted in a potential range of (-1.2 to 1.5 V vs. Ag/AgCl) at a scan rate of 100 mV s⁻¹. After electrolysis, a voltammogram was obtained for the final product cycle considering the highest oxidation peak current. In a reaction that reduces the electrochemical composition of CO₂, the catalyst can direct a specific reaction to produce a certain amount of product. In CO₂RR, the following equation considers the Faraday efficiency (FE) to confirm the selected product during the reaction [37].

$$FE\% = \frac{n_{\text{methanol}} \times n \times F}{\int_0^t I dt} \times 100$$

where, n_{methanol} is the number of moles of formate and n represents the number of electrons transferred from CO₂ to produce one molecule of methanol. In this case, $n = 6$, F is Faraday’s constant (96,485 C mol⁻¹ of electrons), and I is the circuit current (measured by the Potentiostat). Reaction time (t) is measured in s.

3. Result And Discussion

3.1. XRD analysis and Raman spectra

Figure 1 (a) and (b) show the crystal structure of the AFNS NPs, AFNSG NCs and AFNSGT NCs. In the XRD pattern of AFNS, the peaks generally revealed a decent crystal structure and phase. The diffraction peaks were located at $2\theta = 15.63, 31.32, 37.96,$ and 49.85° , which are respectively assigned to the (111), (113), (004) and (115) crystal planes of FNS (JCPDS. 96-900-0979). After combining with graphene, the diffraction peak becomes sharp; the diffraction peak of graphene was observed at $2\theta = 12.63^\circ$, corresponding to the (100) crystal plane. The peak intensity was low because the quantity was low. In the AFNSGT nanocomposite, the XRD peaks of TiO₂ were observed at $2\theta = 25.28, 38.05,$ and 55.02° , which were assigned to the (011), (004) and (121) crystal planes of anatase TiO₂ (JCPDS No.21-1272). The reference XRD data of anatase TiO₂ is shown in Figure 1 (a) and the catalytic activity of the anatase phase is more active than that of the rutile phase, and the electron-hole pair life of anatase is favorable for the surface reaction. The crystallite sizes of each nanocomposite were calculated using the Debye-

Scherrer equation; these were found to be 3.37, 6.31, and 3.68 nm. The average crystallite size of the new-structured ternary nanocomposite is **3.68 nm**, which is higher than the previously studied result of 1.61 nm. A change in the average crystallite size can affect the catalytic activity due to the specialty of the Pechini method. Several previous research papers [38, 39] have analyzed the effect of crystallite size on photocatalytic performance. Figure 1 (b) shows the XRD patterns of the ANS (Ag_2NiS_2), FNS (FeNiS_2) and AFNS NPs, which helps to demonstrate the difference between ternary and quaternary semiconductors. The peaks of NiS, Ag_2S , and FeS were observed in this XRD pattern, as shown in Figure 1 (b). The XRD peaks of AFNS were clear and distinct.

The state of the carbon material (D- and G-band) and molecular interactions between $\text{AgFeNi}_2\text{S}_4$, graphene, and TiO_2 were confirmed by the results of Raman spectroscopy. The full Raman data of the binary and ternary nanocomposites are shown in detail in Figure 1 (c). In AFNSG, graphene had two sharp peaks in the 1348.6 and 1588.2 cm^{-1} shift region, which indicates A_{1g} and E_{2g} symmetry (D- and G-mode). The two types of feature peaks were observed at 1390 and 1583 cm^{-1} [40]. The peak position shifted from the lower to the higher region or vice versa. The quaternary semiconductor had one wide and sharp peak in the 551.5 cm^{-1} region. According to previous studies, chalcogenide-based semiconductors have characteristic peaks in the $100 - 600\text{ cm}^{-1}$ region [41]. Some main peaks were not observed in the current study due to modification of the crystal lattice vibrations of the nanomaterial. AFNSGT included five main peaks, which were assigned to TiO_2 and graphene. The Raman band of anatase-structured TiO_2 was obtained in the $100 - 700\text{ cm}^{-1}$ shift region, which included the E_g , B_{1g} , and A_{1g} modes [42]. The E_g mode peak appeared at 613.5 cm^{-1} , the B_{1g} mode peak was observed at 420.4 cm^{-1} , and the last peak, SEO, appeared at 292.6 cm^{-1} , which indicates the motions of atoms. The characteristic peaks of the quaternary semiconductors were not present in AFNSGT because the symmetric motion of quaternary semiconductors was distorted and the peak intensity of TiO_2 was sharp and strong. The peak position of the D- and G-band was shifted from the higher to the lower shift regions. Shifting of peaks towards a lower or higher wave number is related to chemical bond length. If the chemical bond length of the molecules changes for any internal or external reasons, the wave number may shift. Based on the above theory, the chemical bond length of graphene changed due to the bonding interaction between graphene and TiO_2 . The I_D/I_G ratio was 0.85 in AFNSG and 0.84 in AFNSGT. The change in the value indicated the presence of lattice defects, which arise from the combination of a metal chalcogenide and graphene.

3.2. Morphological analysis

The surface of the photocatalyst was analyzed via SEM. Figure 2 (a) and (b) show the SEM analysis of the quaternary semiconductors, which were wrinkled and elliptical. The preparation of the quaternary semiconductor based on the Pechini method helped to establish a chemical bond between the transition metal and the organic molecules in order to adjust the metal chain. This could demonstrate successful fabrication of the metal chalcogenide semiconductor. After combining with graphene, all particles agglomerated on the graphene exterior owing to the functional group on the graphene surface. The variously structured particles were irregularly agglomerated, as shown in Figure 2 (c)-(d). In the SEM

image of AFNSGT, the TiO_2 particle showed a white, wrinkled and oval structure. Figure 2 (e) and (f) demonstrate the successful fabrication of $\text{AgFeNi}_2\text{S}_4$ -Graphene- TiO_2 . Furthermore, the successful interconnection of $\text{AgFeNi}_2\text{S}_4$, graphene and TiO_2 can be helpful for formation of the hetero-junction structure with good charge carrier properties. The role of graphene is as a bridge and electron acceptor that can support the photogenerated charge carrier and increase the photocatalytic capacity. Figure 2 shows the 3D surface plot, which reveals the roughness of each sample. The surface of AFNS was uneven and sharp, while that of AFNSG was convex. The surface of AFNSGT was smooth and convex.

The internal structure and crystallographic facet of each nanocomposite were analyzed by TEM and HRTEM. Figure 3 (a) shows the presence of the quaternary semiconductor as an elliptical structure on the graphene, which indicates the successful interaction between AFNS and graphene. The morphology of graphene was clear and provided the large surface needed for growth of the metal compound, as shown in Figure S1 (a)-(b). As shown in Figure 3 (d), the pentagonal TiO_2 appeared as a dark black entity that was uniformly spread on the graphene exterior in the AFNSGT ternary nanocomposite. The TiO_2 and quaternary semiconductors were evenly distributed on the surface of graphene. The oxygenated functional group on the graphene exterior prevents the formation of metal or metal oxide agglomerates. Figure 3 (b) and (e) show the HRTEM findings of the crystallographic facets of each nanocomposite. The lattice fringes show the d-spacing values of the quaternary semiconductor and TiO_2 , 0.235 nm and 0.351 nm, respectively, corresponding to the AFNS (201) and TiO_2 (101) crystal planes, as shown in Figure 3 (b) and (e). The average particle size histograms of the binary, ternary and quaternary semiconductors are shown in Figure 3 (c), (f) and (g). The average particle sizes were 3.08 (AFNS in AFNSG), 2.75 (AFNS in AFNSGT), and 3.08 nm (TiO_2 in AFNSGT).

Additionally, quantitative element analysis was done using an EDX instrument. Figure 4 shows the microanalyses of all as-synthesized samples, which reveal the presence of the main elements. Ag, Fe, Ni, S, Ti, and O were obtained from the metal and metal-oxide component, and C was derived from the main adsorbent material, graphene, in the ternary photocatalyst. Each element had its own $K\alpha$ and $K\beta$ values in the appropriate region. These elemental analyses are summarized in the 3D pie graph.

3.3. FTIR and XPS analysis

FTIR was used to identify the presence of the functional groups of the nanocomposites. Figure 5 shows the FTIR results of the nanocomposites. The adsorption band of the carbonyl group (C=O) appeared at 1582.9 cm^{-1} , the carboxylic acid group (-COOH) was observed at 1412.1 cm^{-1} , and asymmetric and symmetric stretching of C-O-C appeared at the wave number regions of 1089.7 and 617.3 cm^{-1} . All of those peaks corresponded to graphene [43]. The blue line reveals the adsorption peaks for AFNS at 2917.8 , 1433.0 , 1117.9 , 998.0 , 665.2 and 622.9 cm^{-1} , which were ascribed to the (R-C(O)-OH), (C(O)-OH), S=O, CH_2 rocking, Fe-O and S-O vibration mode [44]. Most of the peaks were ascribed to the citric acid and the adsorption bands, confirming the successful chemical bonding state of the metal chalcogenide semiconductor. After combination with graphene, the peak intensity and vibration mode changed due to the interaction between graphene and AFNS. In the FTIR spectra of AFNSGT, the wide adsorption band of

the Ti-O-Ti of TiO₂ appeared at 1079.49 and 584.5 cm⁻¹ [45]. The FTIR analysis of the samples confirmed the successful formation of the AgFeNi₂S₄-Graphene-TiO₂ ternary nanocomposite.

XPS was used to analyze the chemical states and interactions among AgFeNi₂S₄, graphene, and TiO₂. Figure 6 shows the XPS spectrum of each element. The binding energy depends on the chemical interactions and form of the samples. Figure 6 (a) shows the XPS survey spectra, which indicated the existence of each element and confirmed the successful formation of AFNSGT. Figure 6 (b) shows two peaks at the 368.35 and 374.37 eV binding regions, which are related to the Ag3d_{5/2} and Ag3d_{3/2} spectra of Ag (I) in AFNSGT [46]. The XPS spectrum of Fe2p (Figure 6 (c)) displayed four deconvoluted peaks at 711.14, 714.89, 724.76, and 731.75 eV. The photoelectron peak at 711.14 eV corresponds to the binding energy of Fe³⁺ 2p_{3/2}, while the peak at 724.76 eV can be assigned to Fe²⁺ 2p_{3/2}. The peak at 731.75 eV corresponds to the 2p_{1/2} of Fe (II) and Fe (III) ions [47]. The last peak, at 714.89 eV, is a satellite peak that indicates the coexistence of Fe (II) and Fe (III) in the quaternary semiconductor. Figure 6 (d) shows that the Ni2p XPS spectrum was deconvoluted into two spin-orbit doublets. The photoelectron peaks at 856.52 and 873.72 eV indicate the 2p_{3/2} and 2p_{1/2} spin orbitals of Ni³⁺. The other two peaks are assigned to the high-spin divalent state (satellite peaks) of Ni²⁺ [48]. The S2p XPS spectrum consisted of four peaks, located at 163.86, 165.04, 169.29, and 170.35 eV, as shown in Figure 6 (e). These four peaks can be assigned to monosulfide (S²⁻) and disulfide (S₂²⁻) [49]. The XPS peaks of sulfide were observed at 158 – 161 eV, and the disulfide peaks were located in the 162 – 168 eV region.

The electron configuration of C1s consists of three peaks, which correspond to the C-C (aliphatic), C-O-C, and C=O groups, as shown in Figure 6 (f) [50]. The high-resolution Ti2p spectrum of AFNSGT displayed two peaks at 459.42 and 465.18 eV, which are related to Ti⁴⁺2p_{3/2} and Ti⁴⁺2p_{1/2}. In addition, the 2p_{3/2} spin-orbitals clearly indicate the presence of Ti (IV); the ratio of these two peaks is 2:1, as shown in Figure 6 (g) [51]. The O1s spectrum is composed of four peaks, located at 530.7, 532.65, 532.69 and 535.34 eV. The first peak is related to the C-O group, whereas the second peak is assigned to the metal-carbonate forms (O-Me), as shown in Figure 6 (h) [52]. The existence of the metal carbonate forms confirms the interaction between metal and oxygen. The next two peaks correspond to the carbonyl and carboxyl groups.

3.4. PL, photocurrent response, Nyquist plot and DRS analysis

The charge transfer and interactions among AFNS, TiO₂, and graphene were studied using the DRS, photocurrent response, PL, and EIS methods. The charge separation capacity of AFNSGT NCs was analyzed by the PL-method. The intensity of PL depends on the recombination rate of the electron-hole pairs; a decrease in PL intensity indicates that the charge carrier has a long lifetime. All photocatalysts showed a light response under the 514 nm laser, as shown in Figure 7 (a). The emission peaks of the samples appeared in the 540 – 660 nm range, in the visible light region. In the PL spectra, two sharp emission peaks appeared, at wavelengths of 546.51 and 551.95 nm. Additionally, pure AFNS NPs and

AFNSG NCs had wide emission peaks near 604.66 nm. The wide-emission peak area and shape changed after the addition of TiO₂ to yield AFNSG NCs. The emission peak of the metal-based composite was classified in two sectors: (1) UV emission (NBE) and (2) visible emission (DF defect) [53]. The rapid charge recombination rate of AFNS is confirmed by the high-intensity PL peak. The PL peak intensity was reduced in AFNSG due to the high conductivity and charge transfer capacity of the 2D-structured graphene. In AFNSGT NCs, the intensity of the peak was somewhat reduced due to the efficient interfacial contact between each part, which bolstered the charge carrier separation. The results of the above analysis show that the proposed ternary nanocomposite, consisting of a metal chalcogenide, graphene and TiO₂, has a high charge carrying capacity. The low PL intensity reflected the recombination rate of electron and holes, which is related to rapid conversion from CO₂ into hydrocarbon fuel.

The photocurrent response of all samples showed repeatable signals in fewer than five on-off cycles, as shown in Figure 7 (b). All nanocomposites had a prompt and stable photocurrent response for each cycle. The photocurrent response decayed in the dark but recuperated within 60 s once the light was turned on. The above procedure can be described in terms of the presence of charge transmission from VB to CB under light irradiation. The 2D-structured graphene had a low current value (2.156×10^{-6} mA/cm²) in each cycle. The pure quaternary nanoparticles (AFNS NPs) had a lower current value (2.818×10^{-6} mA/cm²) in every cycle, which indicated the low separation efficiency of the photo-generated charges. AFNSG NCs had a good photocurrent response (1.091×10^{-5} mA/cm²), a result that depends on the combination between graphene and AFNS NPs, which supports the charge separation and electron flow when the light is on. Among the as-prepared nanocomposites, AFNSGT NCs showed a higher photocurrent response (1.272×10^{-5} mA/cm²) during six on-off cycles of light irradiation. The successful interfacial contact between AFNS NPs, graphene, and TiO₂ leads to efficient separation of photo-generated charges and better catalytic activity for the CO₂-reduction process. The obtained photocurrent response result also supported by the Nyquist plot curves, as expressed in Figure 7 (c). The EIS profile is identical to the charge transfer resistance across the electrode/electrolyte, and the semicircle profile exhibit the conductivity. The Nyquist plot of all samples at room temperature for the frequency range from 5 to 1 mHz with a half-cell. The diameter of the semicircle of AFNSGT NCs was significantly reduced that implying the lower charge transfer resistance and assent to efficient separation and transfer of photogenerated charges. Moreover, the semicircular profile of the AFNSG binary nanocomposite is located between that of AFNS and AFNSGT, depending on the electrical conductivity and interfacial connection of AFNS and graphene. Above photo-electrochemical results substantiated that junction between new-modeled AFNS quaternary nanoparticles, 2D-graphene and TiO₂ led to advance the charge carrier properties and construction of new-labeled photocatalyst for the CO₂-reduction.

Figure 7 (d) shows the DRS spectra of the samples. All samples had light responses in the visible and UV light regions. Figure 7 (e) expresses the bandgap energy value of the unary, binary and ternary nanocomposites. The band gap energy value of each nanocomposite was computed by UV-vis DRS, using Equation [1] [54]:

$$[h\nu F(R_\infty)]^{1/n} = A(h\nu E_g) \quad [1]$$

where E_g is the energy of the band gap, $F(R)$ ($1 - R^2/2R$) is the Kubelka-Munk function, A is the constant of proportionality, and $F(R)$ is the absorption coefficient. $h\nu = hc/\lambda$ is the energy of the incident photon. The calculated band gaps of the three nanocomposites were 2.67, 2.59, and 1.95 eV; the band gap value of AFNSGT was lower than that of AFNS and AFNSG. The band gap energy analysis confirmed that AFNSGT had high catalytic activity and efficiently reduced CO_2 into methanol. Nickel sulfide-based or quantum dot united carbonaceous materials or semiconductor photocatalysts are generally used for H_2 evolution [17–18]. The one-spot and seed-mediated hydrothermal methods and a sol-gel method are commonly used to prepare NiS photocatalysts. The structure of the photocatalyst is the main factor that determines catalytic activity. Recently, ternary structured nanocomposites have become popular in the catalytic field because of their advantages over binary materials, which include strong light absorption rates and enhanced photocatalytic potency. In the last decade, several studies have reported on use of NiS-based photocatalysts for CO_2 reduction under light illumination [17–20].

According to our analysis, the ternary nanocomposite formed successfully and showed a high degree of interconnectivity, highly efficient charge transfer, and suppression of the photogenerated e^- and h^+ recombination rate. Also, the combination of 2D graphene and TiO_2 with a metal semiconductor showed more intimate contact, superior electronic coupling, and a more sensitive photosensitizer, which may lead to better CO_2 reduction under light irradiation. Based on the results of both previous studies and the current study, we assume that the ternary nanocomposite has high photocatalytic activity for CO_2 reduction. Currently, ternary chalcogenide photocatalyst materials are commonly used in CO_2 evolution, including ZnO/ZnSe [55], $\text{WO}_3\text{-TiO}_2/\text{Cu}_2\text{ZnSnS}_4$ [56], and $\text{NiS}/\text{CQDs}/\text{ZnIn}_2\text{S}_4$ [57–58] nanomaterials. $\text{AgFeNi}_2\text{S}_4\text{-Graphene-TiO}_2$ exhibits higher photocatalytic CO_2 conversion activities than did the other ternary chalcogenide photocatalysts. Therefore, a noble metal joined quaternary chalcogenide catalyst can still achieve high-efficiency CO_2 reduction. The utility of TiO_2 in the CO_2 photoreduction test is due to the band gap and the location of the energy band, which is comparable to the CO_2 reduction capacity and H_2O oxidation capacity. Theoretically, redox reactions could be occurring on TiO_2 due to its conduction band energy and valence band energy being available to reduce CO_2 to formic acid and methanol, and to oxidize H_2O to form H^+ . In addition, an NiS-based photocatalyst has p-type semiconductor properties, which are favorable to water oxidation and do not strongly affect CO_2 reduction. The combination of TiO_2 and $\text{AgFeNi}_2\text{S}_4$ was evenly spread across the graphene exterior and the successful interaction of those nanocomposites can determine the band structure and photocatalytic potency of the newly modeled ternary nanocomposite.

3.5. Evolution of CO_2 into methanol

The conversion of CO_2 to methanol was carried out by two different experimental methods, photocatalytic and electrochemical. According to the test results, the newly modeled ternary

nanocomposite had high catalytic activity and successfully reduced CO_2 into methanol. Figure 8 ((a), (c) and (e)) shows the quantification of the final methanol yield under different light conditions. The unary, binary, and ternary nanocomposites were used for the photocatalytic reduction of CO_2 to methanol. The entire test process was carried out under two different conditions, with-scavenger and without-scavenger. The final concentration of methanol was analyzed by the "Quantitative Analysis of Alcohol" method using CrO_3 as a strong oxidizing agent. During the experiment, the final methanol was oxidized, and the oxidation state of CrO_3 decreased. The color of the base solution changed – as the methanol concentration increased, the oxidation state of CrO_3 decreased, and the color of the base solution changed accordingly. Figure 8 (a) shows the final methanol yield over the AFNS unary photocatalyst under different types of light irradiation for 48 hours. Under visible light, the highest methanol yield was 2.339%, in the with-scavenger condition. During UV radiation, the methanol yield increased to 4.136%; this increase in yield was directly related to the effect of ultraviolet photon energy. The band gap value of the AFNS was 2.67 eV, which confirms that the newly modelled quaternary semiconductor showed a light response for both visible and UV light. Figure 8 (b) shows the cyclic voltammogram of the AFNS working electrode in the CO_2 -dissolved solution and the final product at a scan rate of 100 mV s^{-1} . The CV graph occurred in a negative potential range (-0.9 to -0.05 V) on the AFNS working electrode system. The results of the post-electrolysis test show that the highest oxidation peak appeared around 1.20 V (vs. Ag/AgCl). The cyclic voltammogram was performed under pure methanol conditions using the as-prepared working electrodes, and the highest oxidation peaks were found in the potential range of 0.39 to 1.20 V (V vs. Ag/AgCl), as shown in Figure S2. The abovementioned results suggest that unary nanomaterials play an important role in reducing carbon dioxide to methanol. Figures 8 (c) and (d) show the results of methanol production with the AFNSG nanocomposites. The experimental results confirm that the CO_2 conversion efficiency of this catalyst is better than that of the AFNS quaternary nanocomposite. The methanol yields were 3.592% and 4.845% in the without-scavenger condition. The methanol yields were increased to 4.738% and 6.349% in the system with the electron-donor scavenger. In the cyclic voltammogram, the highest oxidation peak appeared at a potential of approximately 1.2 V (vs. Ag/AgCl) and the current density increased.

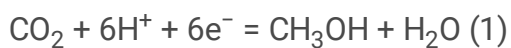
Compared to the unary and binary composites, the ternary composite showed high conversion efficiency for the CO_2 evolution reaction. Continuous production of CH_3OH was obtained using all types of samples, but there was an increasing trend in the evolution of CH_3OH that was directly related to the properties of the photocatalyst. The methanol yields were increased when AFNSGT was used due to the properties of 2D-structured graphene. The graphene increases the light absorption rate and conductivity, which strongly enhances the photocatalytic potency of the AFNSGT ternary nanocomposite. The highest methanol yields were obtained when using AFNSGT nanocomposite; the yields were 5.504 and 5.971% under the without-scavenger condition. The methanol yields increased by approximately 1.5-fold and the highest yields were obtained when using the AFNSGT nanocomposite under light irradiation. The highest methanol evolution of 6.291 and 8.679% was achieved over AFNSGT in the with-scavenger condition. The CV graph appeared in a negative potential range (-0.9 to -0.76 V) in a CO_2 -dissolved solution. In

addition, AFNSGT showed a high CO₂ conversion efficiency in the electrochemical reduction process. In the cyclic voltammogram data, the highest oxidation peaks appeared at 1.18 V (V vs. Ag/AgCl), as shown in Figure 8 (f). The abovementioned CV graph location is the same as that shown in Figure S2. This result suggests that ternary nanomaterials play an important role in reducing carbon dioxide to methanol.

The results of the abovementioned photocatalytic experiments imply that the best CO₂ reduction was obtained in the UV light region, because UV light can supply efficient photon energy which can activate the photocatalyst. To increase the CO₂ reduction and catalytic activity of the nanocomposite, the electron-donor scavenger (Na₂SO₃) was used because it allows CO₂ to combine with water. There are two reasons for this phenomenon: (i) an increase in the amount of dissolved CO₂, and (ii) a reduction in recombination of hole-electron pairs, leading to a longer decay time of surface electrons and facilitation of CO₂ reduction.

Prior to the electrochemical procedure, a 0.04 M NaHCO₃ solution was placed in a sealed three-electrode glass cell and a CO₂-saturated electrolyte was prepared by blowing CO₂ at a pressure of 0.2 kg/cm² for 30 min. Three different types of electrodes were used during the experiment, and the CO₂-dissolved solution was electrolyzed. After electrolysis, a voltammogram was obtained for the final product, considering the highest oxidation peak current. The cyclic voltammogram test was performed under two different conditions: (i) CO₂-dissolved solution before electrolysis, and (ii) methanol solution after electrolysis.

The electrochemical mechanism of CO₂ reduction was determined by analyzing the Faraday efficiency of the final product. According to Equation (1), thermodynamically, 6 electrons are required for the conversion of CO₂ to methanol:

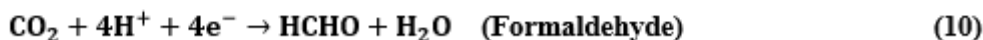
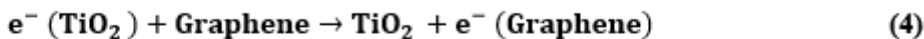
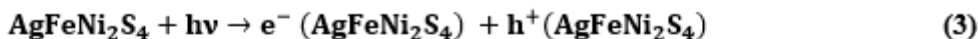
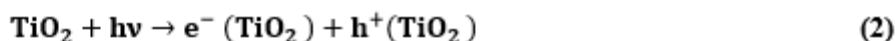


The Faraday efficiency of the quaternary nanocomposite was 25.46%. The value of the Faraday efficiency increased in the AFNSG binary nanocomposite due to the junction of 2D-structured graphene and metal chalcogenide quaternary photocatalyst, and the final calculated efficiency was around 39.97%. The value of the Faraday efficiency for the AFNSGT ternary nanocomposite increased to 44.25%, proving that the successful design of the newly modeled nanocomposite increases the activity of the working electrode and has a positive effect on the electrochemical reduction of CO₂. The peak separation and peak current state depend on the electron transfer properties of the working electrode.

For the electrochemical approach, a solution of 0.04 M NaHCO₃ saturated with CO₂ was electrolyzed on working electrode (vs. Ag/AgCl) and the methanol concentration in the electrolyte solution was determined during a half-time test afterward using a calibration curve via the cyclic voltammetry technique, as shown in in Figure 9. Stability and reusability are the main factors that define the sturdiness of a photocatalyst in practical applications. In the recycling test, the photocatalyst (AFNSGT) was used

four times (192 h) under light irradiation with (0.3 g) and without scavengers in the CO₂ evolution reaction. The ternary photocatalyst was very sturdy during four cycles, with no significant deactivation towards methanol production, as shown in Figure 10. According to the recycling test, the ternary photocatalyst can be considered for generation of solar fuels in practical applications. The recombination rate of the hole-electron pairs is the main parameter that defines the catalytic activity of the photocatalyst. The electron-donor scavenger (sodium sulfite) can reduce the recombination rate of the pairs and increase the number of electrons, while also acting as a sufficient cyclic electron donor. Together, these factors produce a photocatalyst with excellent activity.

FTIR was used to identify the presence of the final products and semi-product. The final methanol product (after 1 and 4 cycles) and commercial methanol solution were used in this FTIR analysis. The FTIR spectrum of methanol, which is shown in Figure S3, consisted of four characteristic peaks located at the theoretical peak region. All key data are summarized in Table S1. The FTIR spectrum of all samples was exhibited in a range of 600 – 3900 cm⁻¹. The peak location and intensity of the reference and methanol products were the same, which confirms that the ternary photocatalyst reduced the CO₂ into methanol. During the test, the semi-product was withdrawn from the reactor and analyzed by FTIR. The results suggest that the chemical structure of CO₂ had changed and confirmed that carbon dioxide can be reduced to methanol. The CO₂ reduction pathway can be described by a chemical reaction, given below. The reduction of CO₂ to methanol involves unique reaction pathways. In general, the reduction of CO₂ requires a more negative potential level in the conduction band (CB), while water oxidation needs a more positive level in the valence band (VB), thereby increasing the number of protons and enhancing the reduction of carbon dioxide. Under Vis/UV light irradiation, both AgFeNi₂S₄ and TiO₂ absorb energy from photons, and electrons are excited from VB to CB. Graphene can accelerate the charge carrier between AFNS and TiO₂ and suppress charge recombination.



Eqs. (2) – (5) describe the activation states of AgFeNi₂S₄, TiO₂, and graphene that enable them to produce photoexcited electron-hole pairs. Eqs. (7) – (11) describe the redox reaction, in which the holes are used for oxidation and the electrons are used for reduction. The positively charged holes reacted with

water to form hydrogen, and this hydrogen source favored the formation of methanol. Meanwhile, the purged CO₂ was adsorbed on the surface of the photocatalyst, so the photo-excited electrons on the surface can reduce/convert the CO₂ into methanol. The conversion of CO₂ into CH₃OH required 6e⁻ /6H⁺.

4. Conclusion

In conclusion, we successfully fabricated a new ternary nanocomposite by the Pechini method. The advantage of the Pechini method is that it allows us to create a chemical interaction between the transition metal and organic molecules to form a metal chain. The morphology, functional groups and electrochemical properties of the unary, binary and ternary nanocomposites were analyzed by spectroscopic techniques. The ternary structured nanocomposite had more stable properties and charge carrier separation due to the presence of 2D-structured graphene, TiO₂ and the quaternary semiconductor. 2D-structured graphene can act as a bridge between the semiconductor (TiO₂) and a quaternary semiconductor that increases light absorption and enhances photo-generated charge transfer. The conduction band structure of TiO₂ makes it available to reduce carbon dioxide to methanol under light irradiation, thus enhancing the catalytic activity of the ternary nanocomposite. The CO₂ reduction process was conducted through photocatalytic and electrochemical methods. The highest methanol evolutions of 6.291 and 8.679% were achieved over AFNSGT, while methanol yields of 4.738 and 6.349% were achieved over the AFNSG nanocomposite in the photocatalytic process. The ternary catalyst was reusable after four cycles, which confirmed that the newly modeled nanocomposite will be useful for practical applications. In electrochemical CO₂ reduction, the Faraday efficiency is the main parameter that defines the performance of the working electrode and the evolution of methanol. The Faraday efficiency of AFNSGT increased to 44.25%, which proves that the successful design of the newly modeled nanocomposite increases the activity of the working electrode and has a positive effect on the electrochemical reduction of CO₂. In this work, we synthesized the AgFeNi₂S₄-Graphene-TiO₂ ternary nanocomposite by the Pechini method. The photocatalytic and electrochemical CO₂ reduction data confirmed that the preparation method, morphological state, and charge carrier properties of the photocatalyst are important for the catalytic activity and efficiency of the methanol evolution pathway. This work confirms that the new structured nanomaterial can be applied to reduce environmental pollution and fabricate hydrocarbon fuels.

Declarations

Acknowledgments

This work was supported by the Research Foundation of Hanseo University in 2021. The authors are grateful to the staff of the University for financial support.

Ethical Approval

We had kept the Ethical fields in all of terms. In this research process, we did not use any illegal and inhibited human test, drug and instrument.

Consent to Participate

We confirm that the manuscript has been read and approved by all named authors and that there are no other persons who satisfied the criteria for authorship but are not listed.

Consent to Publish

We further confirm that the order of authors listed in the manuscript has been approved for this publication by all of us.

Authors Contributions

We understand that the Corresponding Author (Oh W.C) is the sole contact for the Editorial process Oh W.C. (he) is responsible for communicating with the other authors about experimental progress, submissions of revisions, and final approval of proofs. Conceptualization, methodology, formal analysis, and writing process are held by Z.O. We confirm that we have provided a current, correct email address that is accessible by the Corresponding Author, and which has been configured to accept email from.

Funding

For the publication, there has been no significant financial support for this work that could have influenced its outcome.

Competing Interests

We wish to confirm that there are no known conflicts of interest associated with this publication.

Availability of data and materials

We the undersigned declare that this manuscript is original with new data and synthesized novel materials, has not been published before and is not currently being considered for publication elsewhere.

References

1. Xu, F.; Zhang, J.; Zhu, B. CuInS₂ sensitized TiO₂ hybrid nanofibers for improved photocatalytic CO₂ reduction. *J. Appl. Catal. B Environ.* 2018a, 230, 194–202.
2. Habisreutinger, S.N.; Schmidt-Mende, L.; Stolarczyk, J.K. Photocatalytic reduction of CO₂ on TiO₂ and other semiconductors. *J. Angew. Chem. Int. Ed.* 2013, 52 (29), 7372–7408.
3. Windle, C.D.; Perutz, R.N. Advances in molecular photocatalytic and electrocatalytic CO₂ reduction, *Coordinator. Chem. Rev.* 2012, 256, 2562.

4. Qu, Q.; Duan, X.F. One-dimensional homogeneous and heterogeneous nanowires for solar energy conversion *J. Mater. Chem.* 2012, 22, 16171-16181.
5. Thomas, F.H.; Timothy, T.C.; Nicholas, H. F. Life cycle greenhouse gas assessment of a coal-fired power station with calcium looping CO₂ capture and offshore geological storage, *Energ. Environ. Sci.* 2012, 5, 7132.
6. Jiaguo, Y.; Jingxiang, L.; Wei, X.; Peng, Z.; Mietek, J. Enhanced Photocatalytic CO₂-Reduction Activity of Anatase TiO₂ by Co exposed {001} and {101} Facets, *Am. Chem. Soc.* 2014, 136, 25, 8839-8842.
7. Xiang, Q.; Cheng, B.; Yu, J. Graphene-Based Photocatalysts for Solar-Fuel Generation, *Angewandte Chemie Int.Ed.* 2015, 54, 11350.
8. Kondratenko, E.V.; Guido, M.; Baltrusaitis, J.; Larrazábal, G.; Pérez-Ramírez, J. Status and perspectives of CO₂ conversion into fuels and chemicals by catalytic, photocatalytic and electrocatalytic processes, *J. Energ. Environ. Sci.* 2013, 6, 3112.
9. Fu, J., Yu, J., Jiang, C., Cheng, B. g-C₃N₄-based heterostructured photocatalysts, *Adv. Energy Mater.* 2018, 8 (3),1701503.
10. Wang, W.H.; Himeda, Y.; Muckerman, J.T.; Manbeck, G.F.; Fujita, E. CO₂ hydrogenation to formate and methanol as an alternative to photo- and electrochemical CO₂ reduction, *Chem. Rev.* 2015, 115, 12936–12973.
11. Low, J., Yu, J., Ho, W. Graphene-based photocatalysts for CO₂ reduction to solar fuel, *J. Phys. Chem. Lett.* 2015, 6, 4244–4251.
12. Tu, W., Zhou, Y., Zou, Z. Photocatalytic conversion of CO₂ into renewable hydrocarbon fuels: state-of-the-art accomplishment, challenges, and prospects, *Adv. Mater.* 2014, 26, 4607–4626.
13. Jin, J., He, T. Facile synthesis of Bi₂S₃ nanoribbons for photocatalytic reduction of CO₂ into CH₃OH, *Appl. Surf. Sci.* 2017, 39, 364–370.
14. Yu, W.; Chen, J., Shang, T., Chen, L., Gu, L., Peng, T. Direct Z-scheme g-C₃N₄/WO₃ photocatalyst with atomically defined junction for H₂ production, *Appl. Catal. B.* 2017, 21, 693–704.
15. Di, T., Zhu, B., Cheng, B., Yu, J. Xu, J. A direct Z-scheme g-C₃N₄/SnS₂ photocatalyst with superior visible-light CO₂ reduction performance, *J. Catal.* 2017, 352, 532–541.
16. Xinyong, T., Xiaorong, C., Yang, X., Hui, H., Yongping, G., Rui, W., Feng, C.; Wenkui, Z. Highly mesoporous carbon foams synthesized by a facile, cost-effective and template-free Pechini method for advanced lithium–sulfur batteries, *J. Mater. Chem. A*, 2013, 1, 3295.
17. Min, Y.; He, G; Xu, Q.; Chen, Y. Dual-functional MoS₂ sheet-modified CdS branch-like heterostructures with increased photostability and photocatalytic activity, *J Mater Chem A.* 2014, 2, 2578-2584.
18. Devi, S.; Korake, P; Achary, S.N.; Gupta, N.M. Genesis of increased photoactivity of CdS/Nix nanocomposites for visible-light-driven splitting of water, *Int. J. Hydrogen Energy.* 2014, 39, 19424-19433.
19. Zhang, W; Xu, R. Surface engineered active photocatalysts without noble metals: CuS-ZnxCd_{1-x}S nanospheres by one-step synthesis, *Int. J. Hydrogen Energy.* 2009, 34, 8495-8503.

20. Zong, X.; Han, J.; Ma, G.; Yan, H.; Wu, G.; Li, C. Photocatalytic H₂ evolution on CdS loaded with WS₂ as cocatalyst under visible light irradiation, *J. Phys. Chem. C*. 2011, 115, 12202-12208.
21. Lu, Q., Rosen, J., Zhou, Y. et al. A selective and efficient electrocatalyst for carbon dioxide reduction. *Nat Commun*. 2014, 5, 3242.
22. Kendra P.K.; Etosha R.C.; David N.A.; Thomas F.J.; New insight into the electrochemical reduction of carbon dioxide on metallic copper surfaces, *Energy Environ. Sci.*, 2012,5, 7050-7059.
23. Roberts F.S.; Kuhl K.P.; Nilsson A.; High selectivity for Ethylene from carbon dioxide reduction over Copper nanocube electrocatalyst, *Angew. Chem. Int. Ed.*, 2015,54, 5179-5182.
24. Peterson A.A.; Abild-Pedersen F.; Studt F.; Rossmeis J.; Nørskov J.K.; How copper catalyzes the electroreduction of carbon dioxide into hydrocarbon fuels, *Energy Environ. Sci.*, 2010,3, 1311-1315
25. Eda, G.; Fanchini, G.; Chhowalla, M. Large-area ultrathin films of reduced graphene oxide as a transparent and flexible electronic material, *Nat. Nanotechnol*. 2008, 3, 270-274.
26. Stankovich, S.; Dikin, D.A.; Dommett, G.H.B.; Khlhaas, K.M.; Zimney, E.J.; Stach, E.A.; Piner, R.D.; Nguyen, S.T.; Ruoff, R.S. Graphene-based composite materials. *Nature*. 2006, 442, 282-286.
27. Tian, H.; Wan, C.; Xue, X.; Hu, X.; Wang, X. Effective Electron Transfer Pathway of the Ternary TiO₂/RGO/Ag Nanocomposite with Increased Photocatalytic Activity under Visible Light, *Catalysts*. 2017, 7, 156.
28. Tian, H.; Shen, K.; Hu, X.; Qiao, L.; Zheng, W.N. S co-doped graphene quantum dots-graphene-TiO₂ nanotubes composite with increased photocatalytic activity, *J. Alloys Compd*. 2017, 691, 369–377.
29. Huang, H.; Liu, K.; Zhang, Y.; Chen, K.; Zhang, Y.; Tian, N. Tunable 3D hierarchical graphene-BiOI nanoarchitectures: Their in-situ preparation, and highly improved photocatalytic performance and photoelectrochemical properties under visible light irradiation, *RSC Adv*. 2014, 4, 49386-49394.
30. Rajendran, R.; Shrestha, L.K.; Minami, K.; Subramanian, M.; Jayavel, R.; Ariga, K. Dimensionally integrated nanoarchitectonics for a novel composite from 0D, 1D, and 2D nanomaterials: RGO/CNT/CeO₂ ternary nanocomposites with electrochemical performance, *J. Mater. Chem. A*. 2014, 2, 18480-18487.
31. Yan, Y.; Sun, S.; Song, Y.; Yan, X.; Guan, W.; Liu, X.; Shi, W. Microwave-assisted in situ synthesis of reduced graphene oxide–BiVO₄ composite photocatalysts and their increased photocatalytic performance for the degradation of ciprofloxacin, *J. Hazard. Mater*. 2013, 250, 106–114.
32. Stefan, D.; María del, C.A.; Elena, P.; Gonzalo, G. Electrochemical Reduction of Carbon Dioxide on Graphene-Based Catalysts, *Molecules*. 2021, 26(3), 572.
33. Zambaga, O.; Kwang, Y.C.; Oh, W.C. Enhanced photocatalytic activity of CO₂ reduction to methanol through the use of a novel-structured CuCaAg₂Se–graphene–TiO₂ ternary nanocomposite, *New J. Chem.*, 2020,44, 16795-16809.
34. Oh, W.C.; Zhang, F.J. Preparation, and characterization of graphene oxide reduced from a mild chemical method, *Asian J. Chem*. 2011, 23, 875.

35. Zambaga, O.; Kwang, Y.C.; Oh, W.C, Novel Micro and Nanostructure of AgCuInS₂-Graphene-TiO₂ Ternary Composite for Photocatalytic CO₂ Reduction for Methanol Fuel, ACS Omega. 2020, 5, 26389–26401.
36. Ya-hui Y.; Ren-rui X.; Hang L.; Can-jun L.; Wen-hua L.; Fa-qi Z. Photoelectrocatalytic reduction of CO₂ into formic acid using WO_{3-x}/TiO₂ film as novel photoanode, Transactions of Nonferrous Metals Society of China. 2016, 26 (9), 2390-2396.
37. Ensafi, A.A.; Alinajafi, H.A.; Rezaei, B. Pt-modified nitrogen doped reduced graphene oxide: a powerful electrocatalyst for direct CO₂ reduction to methanol. J Electroanal Chem, 2016, 783, 82-89.
38. Xueqin, W.; Lasse, S.; Ren, S.; Stefan, W.; Peter, H.; Aref, M.; Chuanxu, Y.; Yudong, H.; Bo, B.I.; Flemming, B. The influence of crystallite size and crystallinity of anatase nanoparticles on the photo-degradation of phenol, J Catal, 2014, 310, 100-108.
39. Mathias, S.; Murilo, P.; Fernando, A.S.; Juliana M. de Souza e Silva, Italo O.M. Singular effect of crystallite size on the charge carrier generation and photocatalytic activity of nano-TiO₂, Appl. Surf. Sci. 2014, 319, 151-157.
40. Malard, L.M.; Pimenta, M.A.; Dresselhaus, G.; Dresselhaus, M.S. Raman spectroscopy in graphene, Phys. Rep. 2009, 473, 51-87.
41. Pandiaraman, M.; Soundararajan, N. Micro-Raman studies on thermally evaporated Ag₂Se thin films, J. Theor. Appl. Phys. 2012, 6, 7.
42. Pierre, M.K.; Simon, D.; Malik, M.; Chuan, P.L.; Mohamed, M.R.; Diaa, A.R.; Bonex, W.M. Strain and grain size of TiO₂ nanoparticles from TEM, Raman spectroscopy and XRD: The revisiting of the Williamson-Hall plot method, Results Phys. 2018, 9, 628-635.
43. Mohammad, A.H.; Shahryar, M.; Nesa, E. The analysis of linear dose-responses in gamma-irradiated graphene oxide: Can FTIR analysis be considered a novel approach to examining the linear dose-responses in carbon nanostructures?, Radiat Phys Chem, 2020, 176, 109067.
44. Nguyen, T.T., Dang, L. M. Size Effect on the Structural and Magnetic Properties of Nanosized Perovskite LaFeO₃ Prepared by Different Methods, Adv. Mater. Sci. Eng. 2012, 3803-3806.
45. Lei, G.; Changqing, Yi.; Yuanyuan, Luo.; Guotao, D. Facile Synthesis of the Composites of Polyaniline and TiO₂ Nanoparticles Using Self-Assembly Method and Their Application in Gas Sensing, Nanomaterials, 2019, 9, 493.
46. Gondal, M.A.; Suliman, M.A.; Dastageer, M.A.; Gaik-Khuan, C.; Basheer, C.; Dan, Y.; Suwaiyan, A. Visible Light Photocatalytic Degradation of Herbicide (Atrazine) using Surface Plasmon Resonance Induced in Mesoporous AgWO₃/SBA-15 Composite, J. Mol. Catal. A. Chem. 2016, 425, 208-216.
47. Hongliang, P.; Zaiyong, M.; Shijun, L.; Huagen, L.; Lijun, Y.; Fan, L.; Huiyu, S.; Yiliang, Z.; Bingqing, Z. High Performance Fe- and N- Doped Carbon Catalyst with Graphene Structure for Oxygen Reduction, Sci. Rep. 2013, 3(1).
48. Yang, G.; Liwei, M.; Wutao, W.; Shizhong, C.; Zhi, Z.; Hongwei, H.; Weihua, C. Double Metal Ions Synergistic Effect in Hierarchical Multiple Sulfide Microflowers for Increased Supercapacitor Performance, ACS Appl. Mater. Inter. 2015, 7 (7), 4311–4319.

49. Diptiman, D.; Md. Estak, A.; Sumit, M.; Biswajit, M.; Shyamal, K.S. Amorphous molybdenum sulfide quantum dots: an efficient hydrogen evolution electrocatalyst in neutral medium, *J. Mater. Chem. A*. 2016, 40, 15486-15493.
50. Demri, B.; Muster, D. XPS study of some calcium compounds, *J. Mater. Process. Technol.* 1995, 55, 311-314.
51. Pyrgiotakis, G.; Wolfgang, S.M. X-Ray Photoelectron Spectroscopy of Anatase-TiO₂ Coated Carbon Nanotubes, *Solid State Phenom.* 2010, 162, 163-177.
52. Hussein, Z., Ming, H.; Moses, O.T. Ta/TiO₂-and Nb/TiO₂-Mixed Oxides as Efficient Solar Photocatalysts: Preparation, Characterization, and Photocatalytic Activity, *Int. J. Photoenergy.* 2012, 1–9.
53. Zhou, X.; Sun, H.; Zhang, H.; Tu, W. One-pot hydrothermal synthesis of CdS/NiS photocatalyst for high H₂ evolution from water under visible light, *Int. J. Hydrogen Energy.* 2017, 42, 11199-11205.
54. Kumar, S.; Bhunia, S.; Singh, J.; Ojha, A.K. Absence of room temperature ferromagnetism in Fe stabilized ZrO₂ nanostructures and effect of Fe doping on its structural, optical and luminescence properties, *J. Alloy. Compd.* 2015, 649, 348–356.
55. Shuangfang, Z.; Xiaohong, Y.; Yinan, Z. Increased photocatalytic reduction of CO₂ to methanol by ZnO nanoparticles deposited on ZnSe nanosheet, *Chem. Phys. Lett.* 2018, 693 170-175.
56. Adil, R.; Honglie, S.; Azhar, A.H.; Luanhong, S.; Rui, L.; Shusong, C. Studies of Z-scheme WO₃-TiO₂/Cu₂ZnSnS₄ ternary nanocomposite with enhanced CO₂ photoreduction under visible light irradiation, *J. CO₂ Util.* 2020, 37, 260-271.
57. Bingqing, W.; Yao, D.; Zirong, D.; Zhaohui, L. Rational design of ternary NiS/CQDs/ZnIn₂S₄ nanocomposites as efficient noble-metal-free photocatalyst for hydrogen evolution under visible light, *Chinese Journal of Catalysis*, 2019, 40 (3), 335-342.
58. O. Zambaga, W.C. Oh, Photocatalytic CO₂ reduction with Graphene-based semiconductor, *JMMP.* 2019, 10, 127

Figures

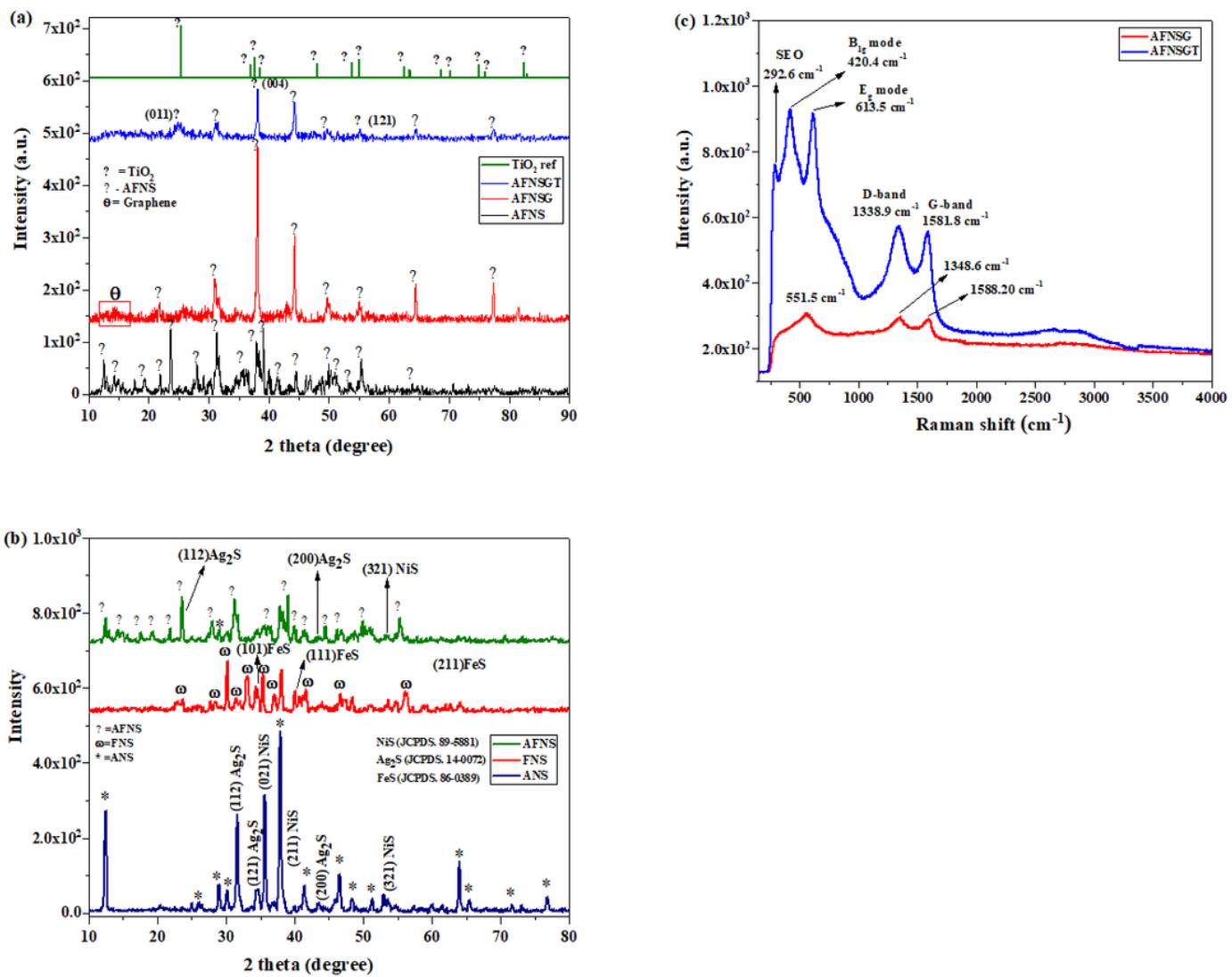


Figure 1

(a) XRD pattern of AFNS NPs, AFNGS and AFNSGT NCs, (b) ANS, FNS and AFNS NCs, (c) Raman spectra (followed by Pechini method).

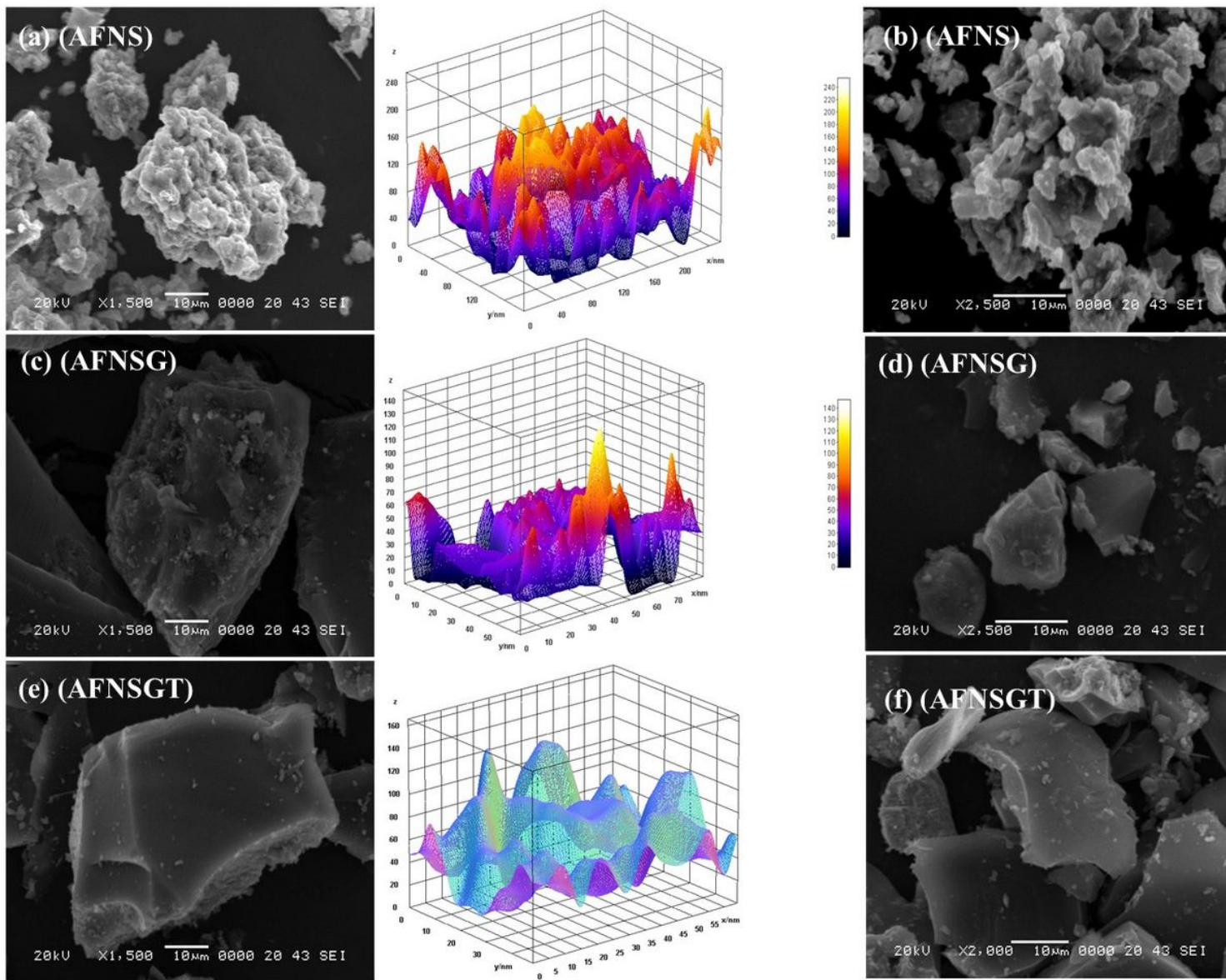


Figure 2

SEM image of (a-b) AFNS NPs, (c-d) AFNSG NCs, (e-f) AFNSGT NCs (followed by Pechini method).

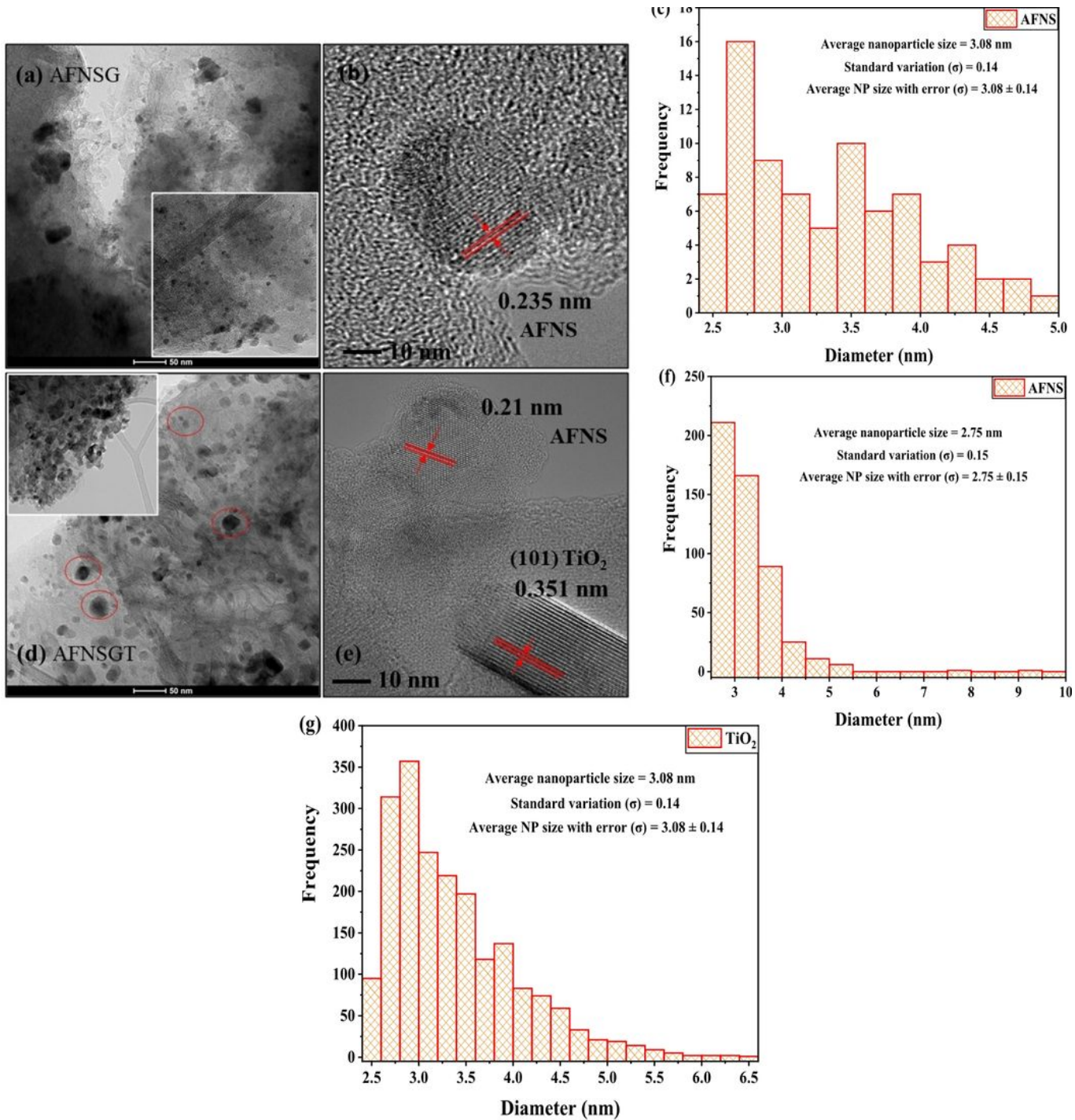
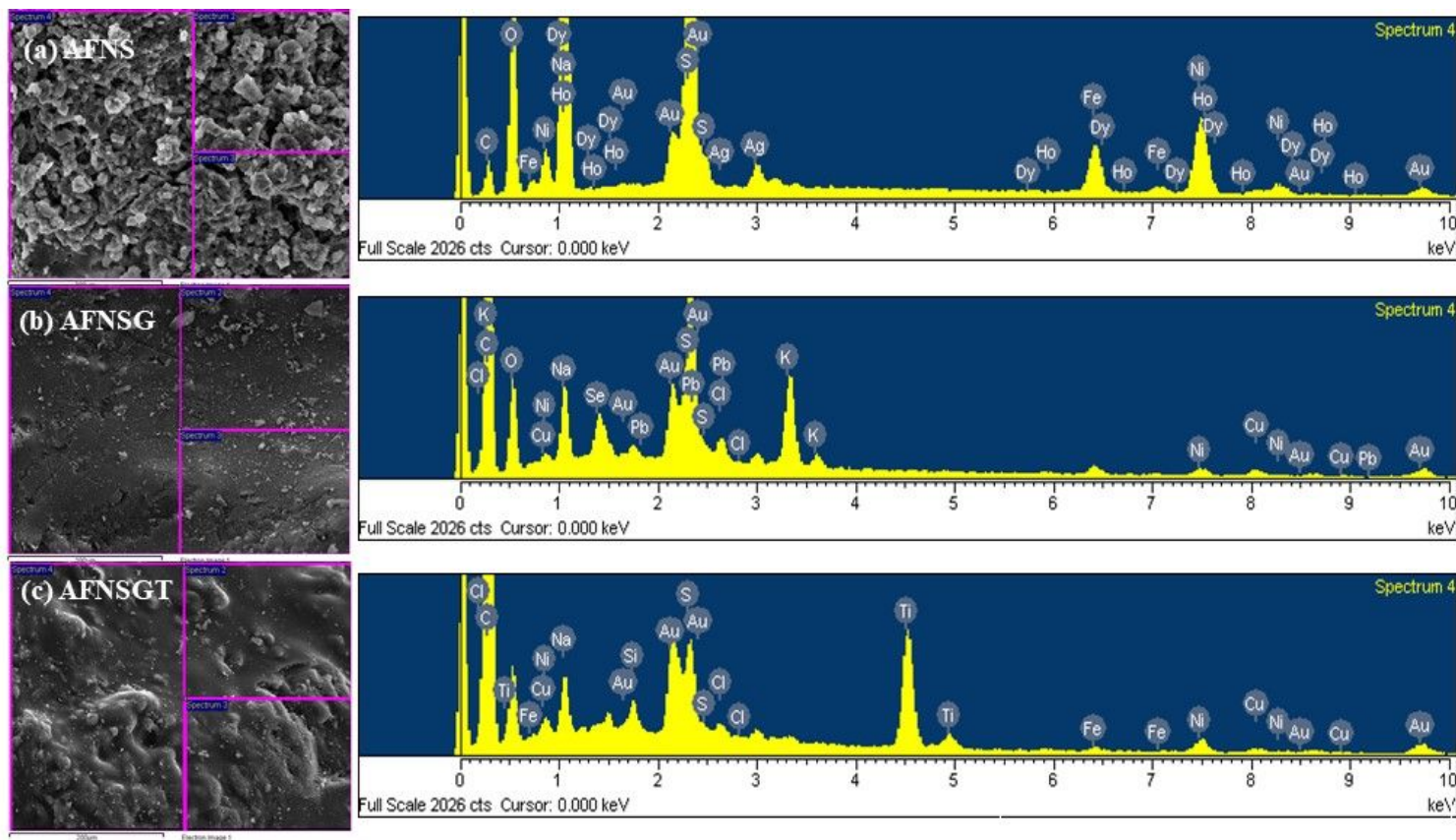
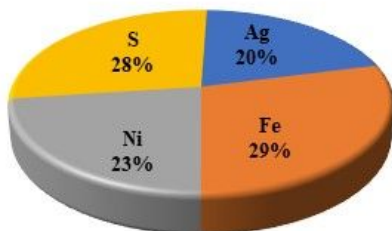


Figure 3

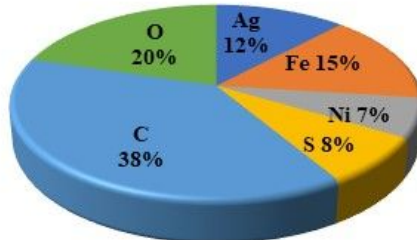
(a, d) TEM images, (b, e) HRTEM images of AFNSG and AFNSGT NCs, (c, f, g) Nanoparticle size histogram of AFNS NPs and TiO_2 in binary and ternary nanocomposites (followed by Pechini method).



(AFNS) Element amount



(AFNSG) Element analysis



AFNSGT Element analysis

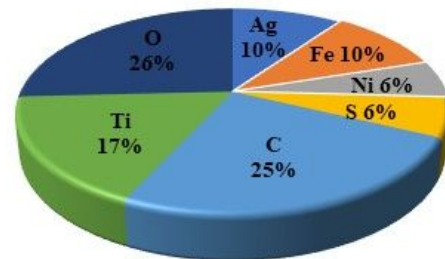


Figure 4

EDX spectrum of AFNS NPs, AFNS NCs and AFNSGT NCs (followed by Pechini method).

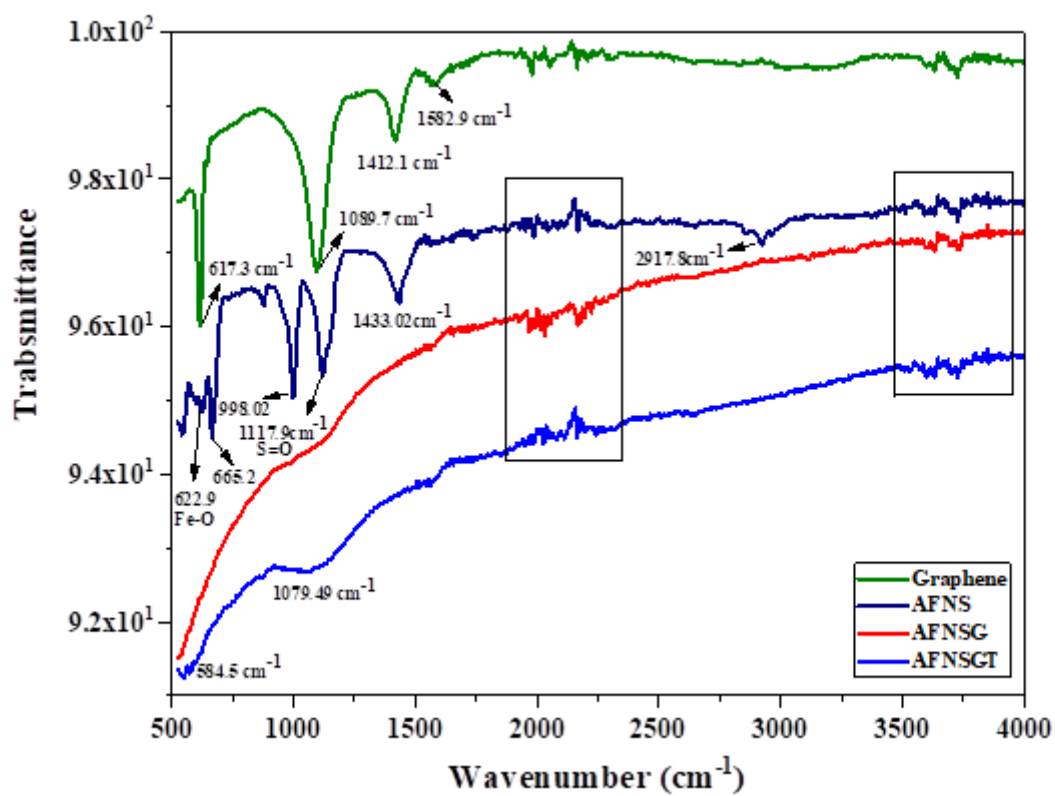


Figure 5

FTIR spectra of the samples.

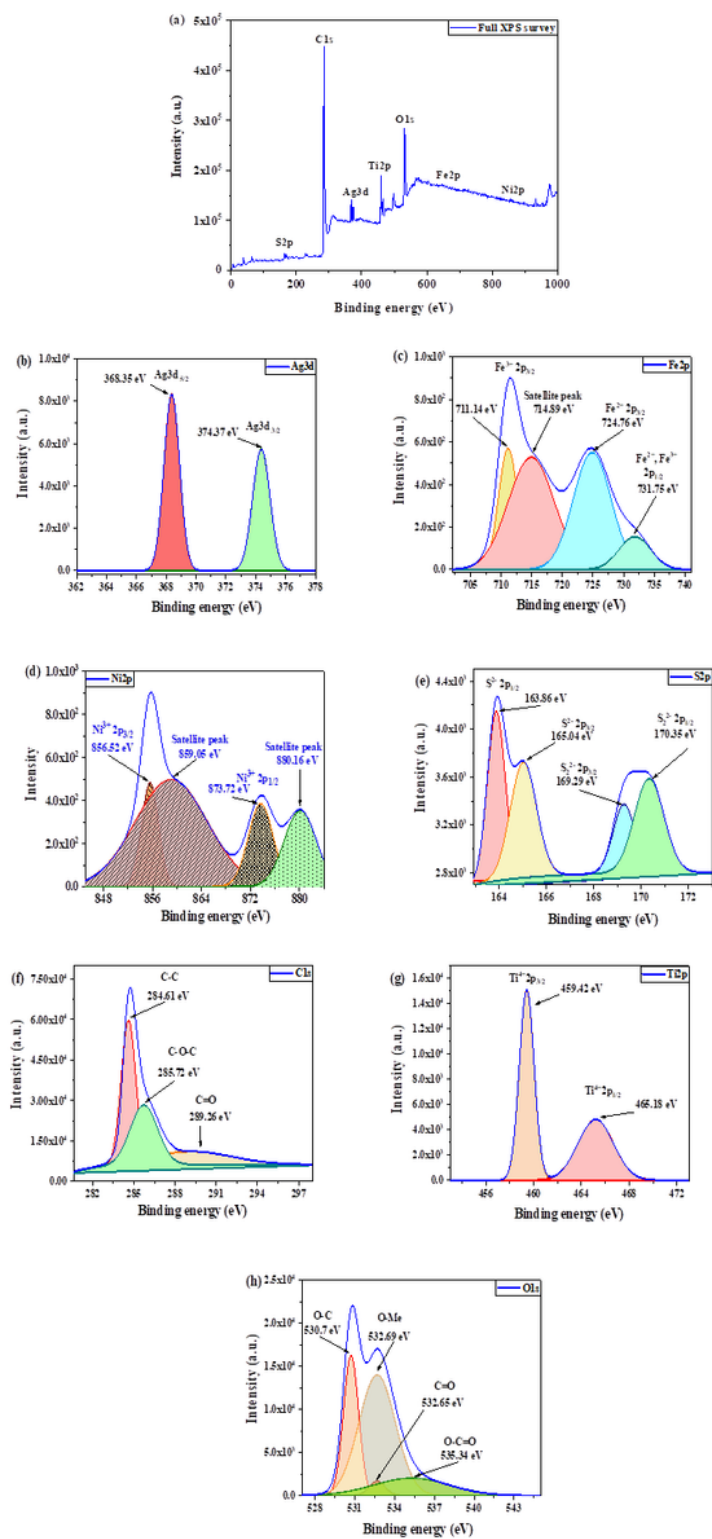


Figure 6

(a) XPS survey spectra and the high-resolution XPS spectra of AFNSGT NCs (synthesized by Pechini method), (b) Ag3d, (c) Fe2p, (d) Ni2p, (e) S2p, (f) C1s, (g) Ti2p and (h) O1s.

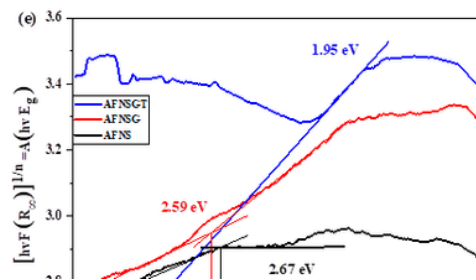
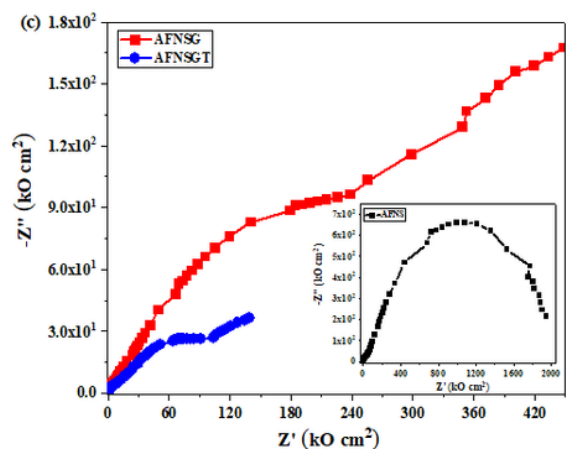
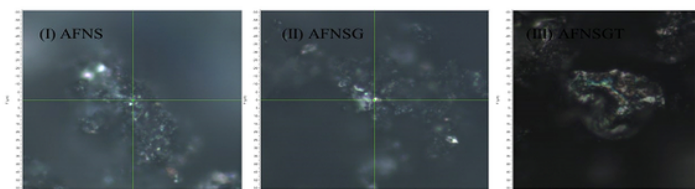
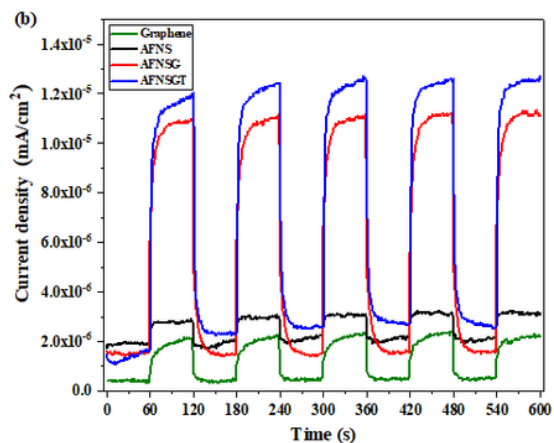
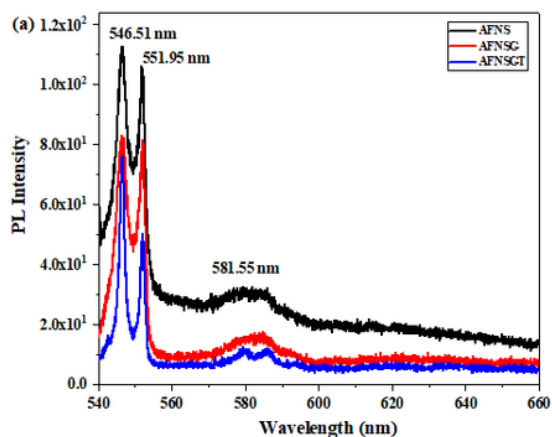


Figure 7

(a) Photoluminescence spectra, (b) Photocurrent response, (c) Nyquist plot, (d) reflectance spectra and (e) DRS of AFNS NPs, AFNSG and AFNSGT NCs (followed by Pechini method).

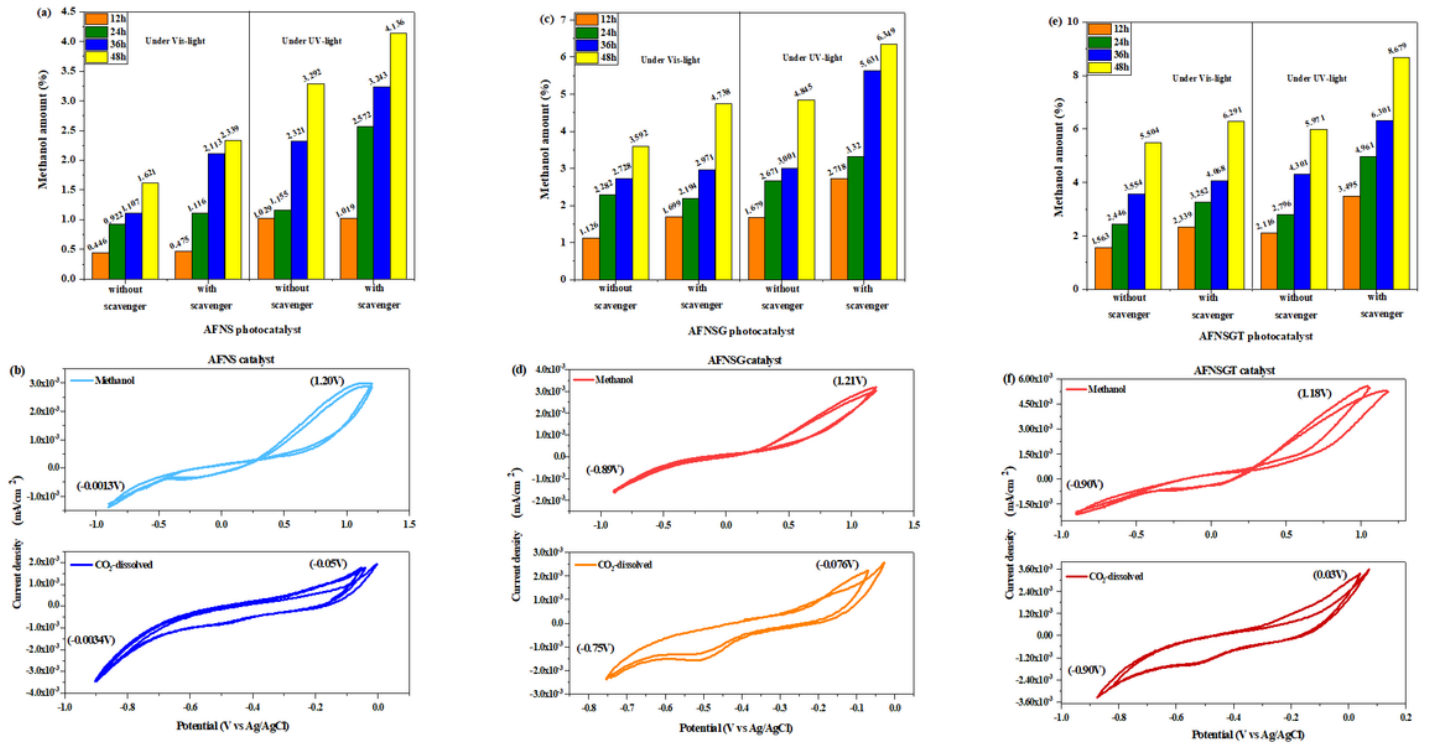


Figure 8

Quantitative analysis of Alcohol result over unary, binary and ternary nanocomposite : effect of scavenger and light irradiation, Cyclic voltammety test of the AFNS NPs, AFNSG and AFNSGT NCs in CO₂ dissolved and after the CO₂ electrolysis (-1.2V to 1.5 V vs Ag/AgCl) under 100 mV s⁻¹ scan rate.

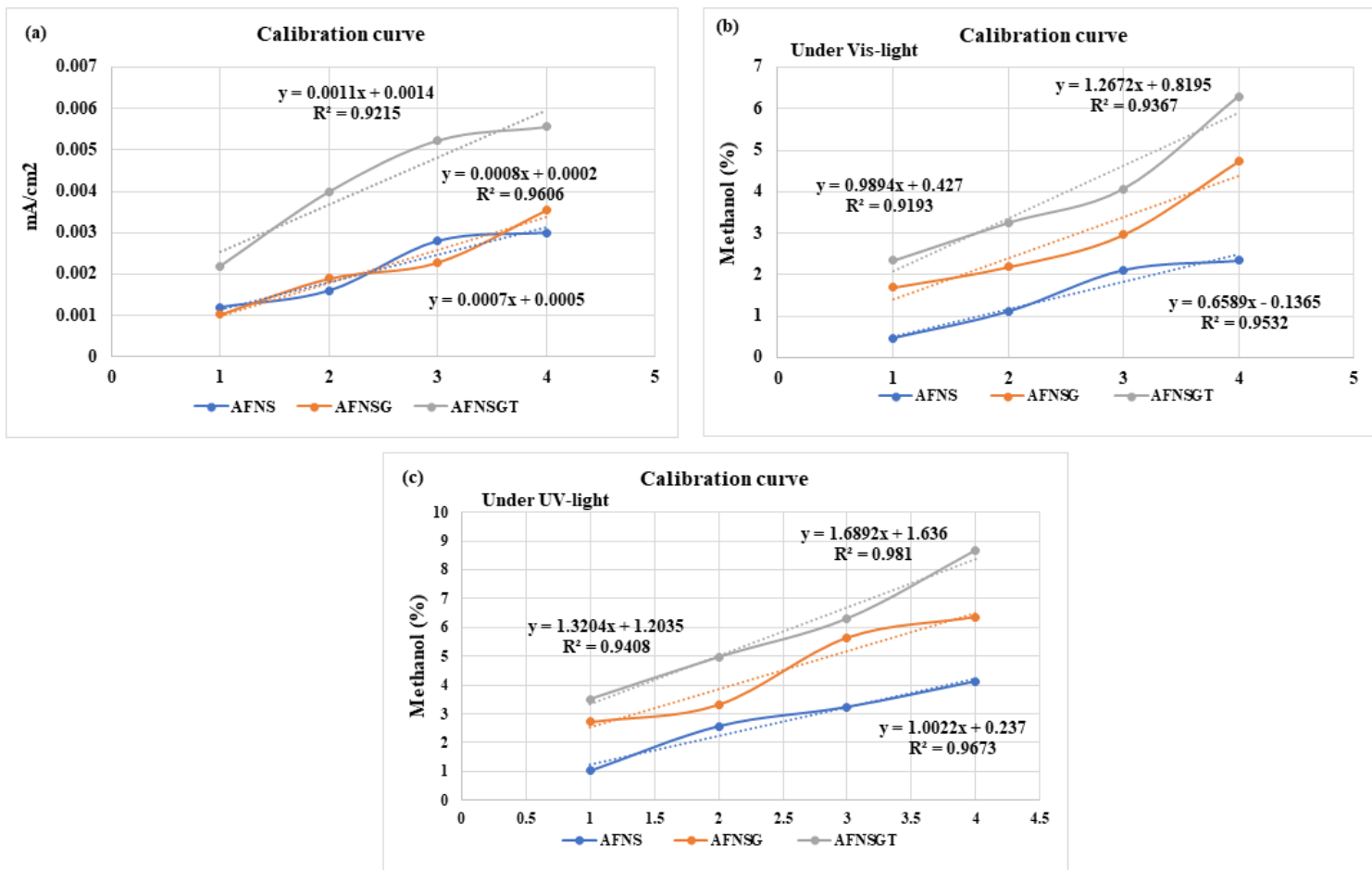


Figure 9

Calibration curve produced by the electrochemical and photocatalytic CO₂ reduction over AFNS NPs, AFNSG and AFNSGT NCs.

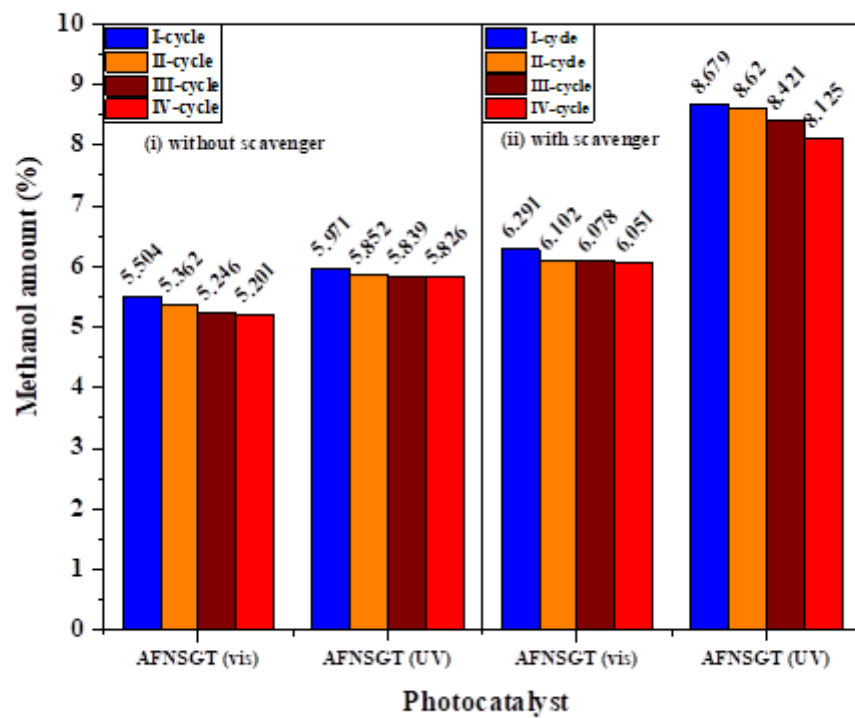


Figure 10

Stability analysis of AFNSGT NCs in multiple cycles (i) without scavenger, (ii) with (0.3 g) scavenger.

Supplementary Files

This is a list of supplementary files associated with this preprint. Click to download.

- [Supplementaryfile220204.docx](#)